LETTER

doi:10.1038/nature11504

The 11 April 2012 east Indian Ocean earthquake triggered large aftershocks worldwide

Fred F. Pollitz[1], Ross S. Stein[1], Volkan Sevilgen[2] & Roland Bürgmann[3]

Large earthquakes trigger very small earthquakes globally during passage of the seismic waves and during the following several hours to days[1–10], but so far remote aftershocks of moment magnitude $M \geq 5.5$ have not been identified[11], with the lone exception of an $M = 6.9$ quake remotely triggered by the surface waves from an $M = 6.6$ quake 4,800 kilometres away[12]. The 2012 east Indian Ocean earthquake that had a moment magnitude of 8.6 is the largest strike-slip event ever recorded. Here we show that the rate of occurrence of remote $M \geq 5.5$ earthquakes (>1,500 kilometres from the epicentre) increased nearly fivefold for six days after the 2012 event, and extended in magnitude to $M \leq 7$. These global aftershocks were located along the four lobes of Love-wave radiation; all struck where the dynamic shear strain is calculated to exceed 10^{-7} for at least 100 seconds during dynamic-wave passage. The other $M \geq 8.5$ mainshocks during the past decade are thrusts; after these events, the global rate of occurrence of remote $M \geq 5.5$ events increased by about one-third the rate following the 2012 shock and lasted for only two days, a weaker but possibly real increase. We suggest that the unprecedented delayed triggering power of the 2012 earthquake may have arisen because of its strike-slip source geometry or because the event struck at a time of an unusually low global earthquake rate, perhaps increasing the number of nucleation sites that were very close to failure.

The 11 April 2012 $M = 8.6$ east Indian Ocean earthquake (Fig. 1a) is by far the largest strike-slip event ever recorded[13]. It was a complex event rupturing a series of subparallel and conjugate faults with dominant moment release within a ~100-s time span[14–19]. This intra-oceanic earthquake precipitated a large, abrupt increase in seismicity worldwide (Fig. 2a). This seismicity reached remote distances of 10,000–20,000 km from the mainshock (Fig. 1b, c), much wider than the near-field aftershock zone surrounding a large mainshock, which is generally a few fault lengths in size[20]. The seismicity jump involved increases in earthquake productivity across a broad magnitude spectrum (Fig. 3). At rates well above background, several $M \geq 5.5$ aftershocks were triggered, unlike those in all previous remote-triggering cases[1–10].

The global distribution of these remote aftershocks is consistent with Love-wave radiation from the mainshock. We consider the square root of the second invariant of the deviatoric strain tensor, ε^{II}, the dynamic shear strain realized during passage of the seismic waves, using a point source convolved with a 100-s-long source time function that replicates observed seismic waveforms (Methods

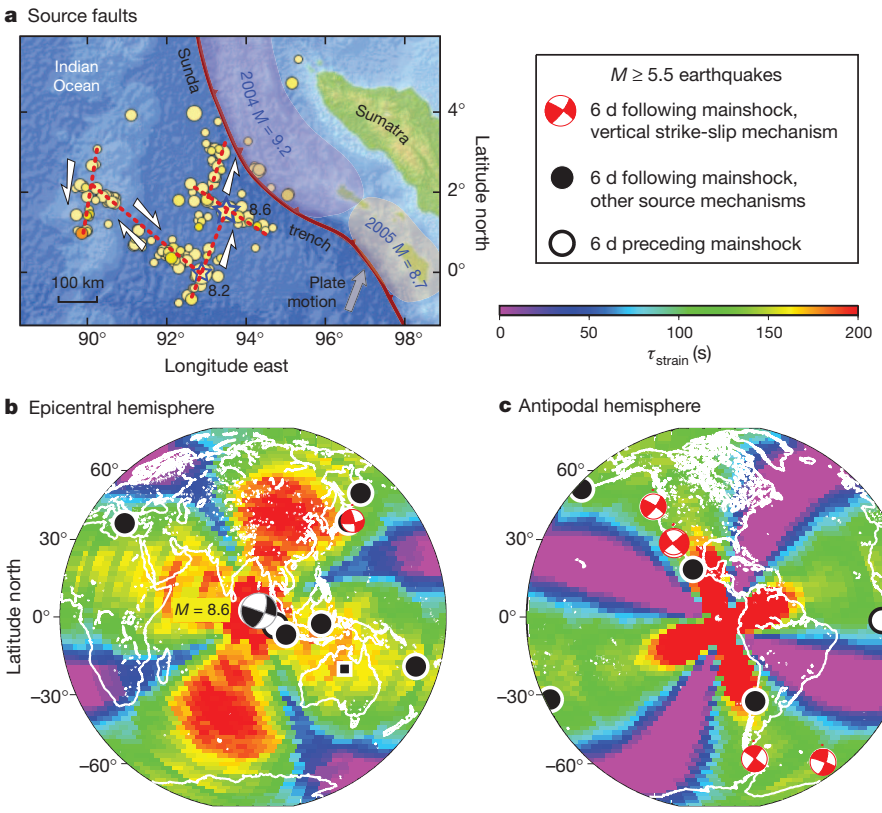

Figure 1 | The 2012 $M = 8.6$ mainshock and $M = 8.2$ aftershock fault ruptures and maps of strain duration τ_{strain} at a threshold value of 0.1 microstrain. a, Inferred fault ruptures of the 11 April 2012 $M = 8.6$ east Indian Ocean earthquake and an $M = 8.2$ aftershock that occurred 2 h later. Superimposed are the first 20 d of $M \geq 4.5$ aftershocks of 0–100-km depth. These earthquakes probably ruptured a complex set of subparallel and conjugate faults with the indicated sense of motion[14–19] (arrows). Parts of the rupture areas of the 2004 $M = 9.2$ and 2005 $M = 8.7$ Nias earthquakes on the Sunda megathrust are indicated. **b**, **c**, Global maps of τ_{strain} (colour scale). Superimposed are the epicentres of $M \geq 5.5$ events that occurred during the 6 d preceding the mainshock (2 epicentres) and following the mainshock (24 epicentres, 16 of which are remote, that is, >1,500 km from the mainshock). Focal mechanisms of six post-mainshock events with near-vertical strike-slip mechanisms (plunge of neutral axis, >60°) are indicated with red beachballs. The 9:00:09 11 April 2012 $M = 5.5$ event (in the western Aleutian Islands) occurred 21 min 33 s after the mainshock between the direct P- and S-wave arrivals from the mainshock; all others are delayed by hours to days. The focal mechanism of the mainshock is plotted at its epicentre.

[1]US Geological Survey, 345 Middlefield Road, MS 977, Menlo Park, California 94025, USA. [2]Seismicity.net, 490 Laurel Street, Suite 10, San Carlos, California 94070, USA. [3]Department of Earth and Planetary Science, University of California, Berkeley, California 94720, USA.

©2012 Macmillan Publishers Limited. All rights reserved

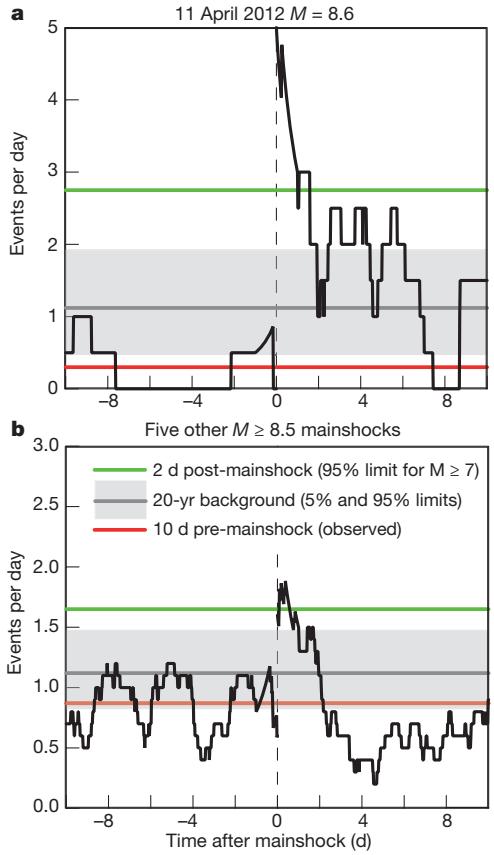

Figure 2 | Global rates of shallow (depth, ≤100 km) $M \geq 5.5$ earthquakes during the 10 d preceding and following a mainshock. Events within 1,500 km of the mainshock are excluded. A running average with a half-width of 1 d is used to construct each curve. Time is relative to the mainshock origin time. **a**, 11 April 2012 $M = 8.6$ east Indian Ocean mainshock. **b**, A collection of five other mainshocks with $M \geq 8.5$. Red horizontal lines denote the $M \geq 5.5$ seismicity rate for the 10 d preceding the 2012 mainshock (**a**) or event-averaged rates for the 10 d preceding the five other mainshocks (**b**). Gray horizontal lines and grey shading denote mean $M \geq 5.5$ seismicity rates and the 5% and 95% empirical probability bounds obtained from analysis of a 20-yr-long NEIC catalogue (Supplementary Fig. 4 and Methods section on background seismicity rates). Green horizontal lines give the 95% empirical upper bounds on R_{post} for one event (**a**) or an aggregate of five events (**b**) derived from a set of catalogue $M \geq 7$ mainshocks (Supplementary Fig. 7).

Summary). We define a first measure of dynamic strain, the 'strain duration' τ_{strain}, as the amount of time that ε^{II} exceeds a threshold value during the wave propagation. Figure 1 reveals that $M \geq 5.5$ aftershocks lie within the four lobes of high τ_{strain} (above a threshold strain of 10^{-7}, or 0.1 microstrain, for >100 s), which coincide with the theoretical lobes of maximum Love-wave excitation for a mainshock of its strike-slip source geometry. A second measure is the peak value of ε^{II} imparted by the mainshock during passage of the seismic waves. Maps of this peak (Supplementary Fig. 1) reveal that $M \geq 5.5$ aftershocks similarly lie within the four lobes of peak dynamic shear strain (>0.25 microstrain). Both measures are important for rationalizing the occurrence of dynamically triggered events[10,21,22].

These unprecedented observations raise the question of whether large aftershocks are always triggered at great distances by large mainshocks. Only very small dynamically triggered remote aftershocks of $M \geq 7$ mainshocks have been found[9], and $M > 5$ aftershocks during the first ~30 h have been found to be triggered only within ~1,000 km from $M \geq 7$ mainshocks[11] (generally within the range of static Coulomb stress triggering), suggesting that the global hazard of large aftershocks does not increase following even a large mainshock. Thus, the $M = 8.6$ east Indian Ocean triggering is probably quite rare.

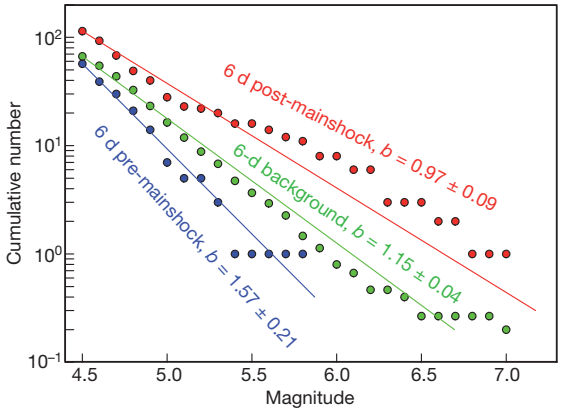

Figure 3 | Cumulative number of global $M \geq 4.5$ events of depth ≤100 km during the 6 d before and after the 2012 event. Both the pre-mainshock (blue symbols) and the post-mainshock (red symbols) seismicities are restricted to be remote (>1,500 km from the mainshock). Superimposed is the cumulative number of background 'remote' events in an average 6-d interval during the year preceding the 2012 mainshock (green symbols). Lines illustrate the corresponding b values from the Gutenberg–Richter law and standard deviations derived using maximum-likelihood regression.

To confirm that the global rate increase is real, we test the null hypothesis that the rate of remote $M \geq 5.5$ events is the same for periods before and after $M \geq 8.5$ mainshocks (Table 1), including the 2012 east Indian Ocean earthquake. The remoteness criterion is defined with a simple distance threshold from the mainshock centroid and is applied uniformly to both pre-mainshock and post-mainshock seismicity. Because the enhancement of dynamically triggered seismicity is thought to take place on a 1–2-d timescale[11], we test whether the average rate of remote $M \geq 5.5$ aftershocks in the 2 d following a mainshock, R_{post}, is the same as the rate, R_{pre}, of 'remote' $M \geq 5.5$ events in the 10 d preceding the mainshock. We use 2 d post-mainshock because of the observed duration of the rate increase and 10 d pre-mainshock to obtain a reliable background rate. Results are similar using other pre-mainshock windows, and here we address the statistical fluctuations in pre-mainshock rates to be expected from the chosen time window. We define the rate change to be

$$\Delta R = R_{post} - R_{pre} \quad (1)$$

and test the null hypothesis by comparing the observed ΔR with empirical probability distributions of ΔR derived from Monte Carlo sampling of the 20-yr global US National Earthquake Information Center (NEIC) catalogue of $M \geq 5.5$ earthquakes (see Methods sections on magnitude of completeness and seismicity rate change).

There is a fivefold increase in the rate, R, of shallow global $M \geq 5.5$ events for several days following the 2012 mainshock (Fig. 2a). A similar but weaker rate change is observed for a collection of five other $M \geq 8.5$ mainshocks during the past decade (Fig. 2b and Table 1), exceeding the 10-d-average pre-mainshock rate by a factor of two for 2 d. The jump in seismicity rate is not attributable to induced mainshock–aftershock sequences (that is, aftershocks triggering aftershocks) and is also apparent over longer time intervals (Supplementary Fig. 2).

Table 1 | $M \geq 8.5$ earthquakes

Date (dd/mm/yyyy)	Magnitude*	Region/name	Tectonic environment	Sense of slip
26/12/2004	9.2†	Sumatra	Sunda megathrust	Thrust + strike slip
28/03/2005	8.7†	Nias	Sunda megathrust	Thrust
12/09/2007	8.5	Sumatra	Sunda megathrust	Thrust
27/02/2010	8.8	Maule, Chile	Andean trench	Thrust
11/03/2011	9.0	Tohoku, Japan	Japan trench	Thrust
11/04/2012	8.6	East Indian Ocean	Intraplate	Strike slip

* From NEIC catalogue unless otherwise noted.
† Ref. 32.

©2012 Macmillan Publishers Limited. All rights reserved

The rate change ΔR provides a test of the null hypothesis. As summarized in Methods, we consider the set of 243 shallow-focus $M \geq 7$ mainshocks that occurred during the 20 yr before the 2012 $M = 8.6$ event; the magnitude of completeness is 5.5 (Supplementary Fig. 3). For a single mainshock, the 95% upper bound on the empirical probability distribution of ΔR is 1.25 events per day. The observed rate increase for the 2012 $M = 8.6$ mainshock (Fig. 2a) is $\Delta R = 2.7$ events per day, which far exceeds the 95% empirical bound. An increase ΔR exceeding 2.5 events per day is not found for any $M \geq 7$ mainshock in the 1992–2012 catalogue (Supplementary Fig. 5). If the search is extended back to 1982, then a ΔR value exceeding 2.5 events per day occurs for only one out of 337 $M \geq 7$ mainshocks in the catalogue (the 5 April 1990 $M = 7.4$ normal-faulting Mariana Islands earthquake). If remote $M \geq 5.5$ events are assumed to occur with a Poissonian probability distribution, then one out of 337 mainshocks translates into a 0.3% probability of the 2012 rate increase occurring by chance.

For the aggregate of five other $M \geq 8.5$ mainshocks, the 95% bound on the empirical probability distribution of ΔR is 0.55 events per day (Supplementary Fig. 6). The observed rate increase (Fig. 2b) is $\Delta R = 0.63$ events per day, a weaker signal than the 2012 rate increase. Thus, the null hypothesis can be rejected at the 99.7% level for the 2012 $M = 8.6$ mainshock and at the 95% level for the aggregate of five other very large mainshocks.

The global nature of the delayed triggered seismicity following the east Indian Ocean earthquake and its association with the Love-wave radiation pattern raise a number of issues. The first is whether strike-slip earthquakes promote triggering of moderate global aftershocks more than thrust sources. The 2012 event is the only $M \geq 8.5$ mainshock with a predominantly strike-slip mechanism (Table 1). A strike-slip event will generate horizontally polarized shear-wave (SH- and Love-wave) energy in four dominant directions, along and perpendicular to the fault strike[23]. Love waves will preferentially stress near-vertical strike-slip faults. Six of the 16 (37%) remote aftershocks of the 2012 event were strike-slip events on near-vertical faults (Fig. 1), whereas the background rate of $M \geq 5.5$ strike-slip events is 24%; four of the strike-slip aftershocks were among the six that occurred during the first 2 d (67%). In contrast, low-angle thrust events generate predominantly P–SV-wave energy with smaller azimuthal variation of radiated energy[23]. For example, the 2004 $M = 9.2$ Sumatra and 2005 $M = 8.7$ Nias earthquakes occurred near the 2012 $M = 8.6$ event but produced smaller remote seismic displacements (Supplementary Fig. 10). Assuming that dynamic strain scales with displacement[24], this qualitatively suggests an enhanced triggering potential for the 2012 event.

A strike-slip source geometry, however, is of secondary importance to earthquake magnitude. We examined the next-largest strike-slip sources of the past 15 yr (the 23 December 2004 $M = 8.1$ Tasman Sea and 28 March 1998 $M = 8.1$ Antarctic earthquakes, both of which were about five times smaller than the 2012 $M = 8.6$ event), but we do not find any increase in remote $M \geq 5.5$ seismicity. Nor do we see (using the Centennial Earthquake Catalog[25]) remote $M \geq 7$ aftershocks following the 1905 $M = 8.4$ Mongolian earthquake doublet.

The triggered aftershocks are not preferentially located in the near-field, where dynamic strain magnitudes are high, but rather are distributed uniformly over the globe (Fig. 1 and Supplementary Figs 1 and 8a). The strain duration (Fig. 1) is more uniformly distributed globally than the peak strain amplitude (Supplementary Fig. 1). This suggests that a dynamic strain threshold enables triggering, as suggested previously[21], and reinforces the notion that dynamic triggering depends on not only the amplitude of transient dynamic strains but also the duration for which they are applied[8,22]. Small events triggered by passage of seismic waves from the 2011 Tohoku earthquake are also distributed globally, with no preference for the near-field region[10], suggesting that dynamic triggering, whether instantaneous or delayed, depends on more than dynamic strain amplitude.

The second issue is the nature of the mechanism behind the delayed triggering of large aftershocks. When compared with the near-instantaneous surface-wave triggering of small global aftershocks, the 2–6-d timescale of global large aftershock activity implies a longer nucleation process. Near-instantaneous triggering of undetected foreshocks or slow-slip transients could initiate a cascade process culminating in earthquakes[26]. Surface waves from large earthquakes have been found to trigger deep-seated non-volcanic tremor in several subduction zones and on the San Andreas fault[27]. This non-volcanic tremor is believed to be associated with slow slip.

The third issue is whether the large jump in global seismicity following the 2012 earthquake is related to the very low seismicity rate preceding it. The 2012 quake struck after 6–12 d of exceptionally low global seismicity (Fig. 4 and Methods section on low pre-earthquake seismicity rate). We suspect that because the dynamic stress is oscillatory and brief, only faults very close to failure can be triggered. If earthquake nucleation sites age, or are stressed towards failure, at a roughly constant rate, then when a period of such extremely low

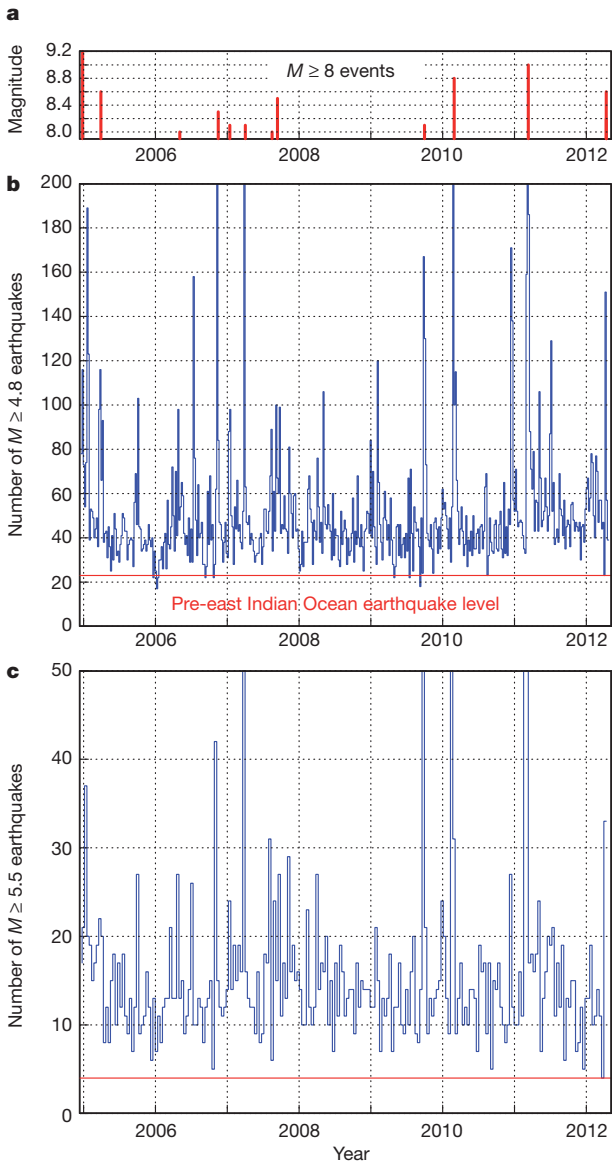

Figure 4 | Global seismicity rates during the 7.3 yr between the 2004 Sumatra earthquake and the 2012 east Indian Ocean earthquake. **a**, Magnitude of $M \geq 8$ events. **b**, **c**, Seismicity rates for $M \geq 4.8$ events in 6-d bins (**b**) and $M \geq 5.5$ events in 12-d bins (**c**). Catalogue is unedited; for example, no 1,500-km exclusion zones are used.

©2012 Macmillan Publishers Limited. All rights reserved

seismicity coincides with a great mainshock, there is a large reservoir of nucleation sites that are critically stressed or very close to failure. In contrast, none of the other $M \geq 8.5$ earthquakes is preceded by such a 6–12-d low background rate. Some of the close-to-failure sites may lie in aftershock zones of local mainshocks, such as one that is an aftershock of the 20 March 2012 $M = 7.4$ Mexican-trench event (Fig. 1).

The strongest evidence for delayed global triggering is provided by the preponderance of strike-slip post-mainshock events (Fig. 1), the jump in seismicity rate in individual regions (for example the Gulf of California (Supplementary Fig. 11)) and the observation that the $M \geq 5.5$ seismicity rate increase is part of a broader global $M \geq 4.5$ rate increase (Fig. 3), which involves large numbers of remote events (114 post-mainshock versus 57 pre-mainshock for 6-d periods).

The above considerations provide only partial answers to the question of why the 2012 event triggered so many remote large aftershocks. The apparent dependence of dynamic triggering on period, with longer periods having greater influence than shorter periods both experimentally and observationally[8,22,28], may be relevant for remote triggering because long-period waves undergo less intrinsic attenuation than do short-period waves. Directivity effects may also prove to be important[29]. Although these and other issues are speculative at this stage, the 2012 east Indian Ocean event has already shown that the phenomenon of remote earthquake triggering is not restricted to small earthquakes or tremor but extends to potentially damaging ($M \approx 7$) earthquakes. This carries implications for the effect of a large earthquake on the global seismic hazard, as the 2012 event caused strong on-land shaking (with a modified Mercalli intensity greater than or equal to seven) in Indonesia, Japan and Mexico.

METHODS SUMMARY

Determination of earthquake rates. We consider global rates, R, of shallow (depth, $\leq$100 km) $M \geq 5.5$ earthquakes during the 10 d preceding and following a given mainshock. These rates exclude pre-mainshock and post-mainshock events within a spherical cap of radius 1,500 km centred on the mainshock centroid. A running average in time is used to count events. For a target time t_{pre} preceding the event, the events are summed in bins spanning a time interval $(t_{pre} - 1\,d, \min\{t_{pre} + 1\,d, 0\})$, where time is relative to the mainshock origin time. For a target time t_{post} following the event, the events are summed in bins spanning a time interval $(\max\{t_{post} - 1\,d, 0\}, t_{post} + 1\,d)$. This procedure is applied to the 11 April 2012 mainshock or an aggregate of $M \geq 8.5$ mainshocks in which the rates are divided by the number of mainshocks used. With the above prescription, the 2-d-average post-mainshock R value is the running-average R value evaluated at $t = 1$ d; this is the post-mainshock rate, R_{post}, used to define the seismicity rate change in equation (1).

Measure of dynamic strain. Long-period synthetic seismograms of length 2 h 33 min are calculated at 10-km depth at each of 5,150 points distributed globally for a point-source representation of the mainshock[30] convolved with a source time function consisting of a cosine ramp function of duration 100 s. They are consistent with observed seismograms (Supplementary Fig. 9). At each point, seismograms for the six components of the strain tensor are converted into time series of ε^{II}, the square root of the second invariant of the deviatoric strain tensor[31]. We define τ_{strain} to be the period during which $\dot{\varepsilon}^{II}$ is greater than a threshold value of 0.1 microstrain, using the time series of ε^{II}.

Full Methods and any associated references are available in the online version of the paper.

Received 20 May; accepted 16 August 2012.
Published online 26 September 2012.

1. Hill, D. P. *et al.* Seismicity in the western United States remotely triggered by the M7.4 Landers, California, earthquake of June 28, 1992. *Science* **260,** 1617–1623 (1993).
2. Kilb, D., Gomberg, J. & Bodin, P. Triggering of earthquake aftershocks by dynamic stresses. *Nature* **408,** 570–574 (2000).
3. Gomberg, J., Reasenberg, P., Bodin, P. & Harris, R. Earthquake triggering by transient seismic waves following the Landers and Hector Mine, California earthquakes. *Nature* **411,** 462–466 (2001).
4. Prejean, K. *et al.* Remotely triggered seismicity on the United States west coast following the M_w 7.9 Denali Fault earthquake. *Bull. Seismol. Soc. Am.* **94,** S348–S359 (2004).
5. Gomberg, J., Bodin, P., Larson, K. & Dragert, H. Earthquake nucleation by transient deformations caused by the $M = 7.9$ Denali, Alaska, earthquake. *Nature* **427,** 621–624 (2004).
6. Husen, S., Taylor, R., Smith, R. B. & Healser, H. Changes in geyser eruption behavior and remotely triggered seismicity in Yellowstone National Park produced by the 2002 M7.9 Denali Fault earthquake, Alaska. *Geology* **32,** 537–540 (2004).
7. Pankow, K. L., Arabasz, W. J., Pechman, J. C. & Nava, S. J. Triggered seismicity in Utah from the November 3, 2002, Denali Fault earthquake. *Bull. Seismol. Soc. Am.* **94,** S332–S347 (2004).
8. Brodsky, E. E. & Prejean, S. G. New constraints on mechanisms of remotely triggered seismicity at Long Valley Caldera. *J. Geophys. Res.* **110,** B04302 (2005).
9. Velasco, A. A., Hernandez, S., Parsons, T. & Pankow, K. Global ubiquity of dynamic earthquake triggering. *Nature Geosci.* **1,** 375–379 (2008).
10. Gonzalez-Huizar, H., Velasco, A. A., Peng, Z. & Castro, R. R. Remote triggered seismicity caused by the 2011 M9.0 Tohoku-Oki, Japan earthquake. *Geophys. Res. Lett.* **39,** L10302 (2012).
11. Parsons, T. & Velasco, A. A. Absence of remotely triggered large earthquakes beyond the mainshock region. *Nature Geosci.* **4,** 312–316 (2011).
12. Lin, C.-H. Remote triggering of the Mw 6.9 Hokkaido Earthquake as a Result of the Mw 6.6 Indonesian Earthquake on September 11, 2008. *Terr. Atmos. Ocean Sci.* **23,** 283–290 (2012).
13. McGuire, J. & Beroza, G. A rogue earthquake off Sumatra. *Science* **336,** 1118–1119 (2012).
14. Kiser, E. Preliminary Rupture Modelling of the April 11, 2012 Sumatran Earthquakes. http://www.seismology.harvard.edu/research_sumatra2012.html (2012).
15. Wang, D., Mori, J. & Ohmi, S. Rupture Process of the April 11, 2012 Sumatra (Mw 8.6) Earthquake Imaged with Back-Projection of Hi-net Data. http://www.eqh.dpri.kyoto-u.ac.jp/src/etc/sumatra.htm (2012).
16. Meng, L. Ampuero, J.-P., Duputel, Z., Luo, Y. & Tsai, V. C. Earthquake in a maze: compressional rupture branching during the 2012 M_w 8.6 Sumatra earthquake. *Science* **337,** 724–726 (2012).
17. Incorporated Research Institutions for Seismology. Back projections for MW 8.7 off W coast of Northern Sumatra. http://www.iris.edu/spud/backprojection/118733 (2012).
18. Yue, H., Lay, T. & Koper, K. D. *En échelon* and orthogonal fault ruptures of the 11 April 2012 great interplate earthquake. *Nature* http://dx.doi.org/10.1038/nature11492 (this issue).
19. Delescluse, M. *et al.* Intra-oceanic seismicity off Sumatra boosted by the Banda–Aceh megathrust. *Nature* http://dx.doi.org/10.1038/nature11520 (this issue).
20. Kanamori, H. The energy release in great earthquakes. *J. Geophys. Res.* **82,** 2981–2987 (1977).
21. Gomberg, J. & Johnson, P. Dynamic triggering of earthquakes. *Nature* **437,** 830 (2005).
22. Hill, D. P. & Prejean, S. in *Earthquake Seismology* (ed. Schubert, G.) 258–288 (Treatise on Geophysics 4, Elsevier, 2007).
23. Dahlen, F. A. & Tromp, J. *Theoretical Global Seismology* Ch. 11 (Princeton Univ. Press, 1998).
24. Gonzalez-Huizar, H. & Velasco, A. A. Dynamic triggering: stress modeling and a case study. *J. Geophys. Res.* **116,** B02304 (2011).
25. Engdahl, E. E. & Villaseñor, A. in *International Handbook of Earthquake and Engineering Seismology* (ed. Lee, W. H. K.) 665–690 (Academic, 2002).
26. Shelly, D. R., Peng, Z., Hill, D. P. & Aiken, C. Triggered creep as a possible mechanism for delayed dynamic triggering of tremor and earthquakes. *Nature Geosci.* **4,** 384–388 (2011).
27. Peng, Z. & Gomberg, J. An integrated perspective of the continuum between earthquakes and slow-slip phenomena. *Nature Geosci.* **3,** 599–607 (2010).
28. Peng, Z., Vidale, J. E., Wech, A. G., Nadeau, R. M. & Creager, K. C. Remote triggering of tremor along the San Andreas fault in central California. *J. Geophys. Res.* **114,** B00A06 (2009).
29. Velasco, A. A., Ammon, C. J., Farrell, J. & Pankow, K. Rupture directivity of the November 3, 2002 Denali Fault earthquake determined from surface waves. *Bull. Seismol. Soc. Am.* **94,** S293–S299 (2004).
30. Koss, H. & Nettles, M. Global CMT Project Moment Tensor Solution: April 11, 2012, Off W Coast of Northern Sumatra, MW = 8.6. http://earthquake.usgs.gov/earthquakes/eqinthenews/2012/usc000905e/neic_c000905e_gcmt.php (2012).
31. Jaeger, J. C. & Cook, N. G. W. *Fundamentals of Rock Mechanics* Vol. 33 (Chapman and Hall, 1984).
32. Chlieh, M. *et al.* Coseismic slip and afterslip of the Great (Mw 9.15) Sumatra-Andaman earthquake of 2004. *Bull. Seismol. Soc. Am.* **97** (1a), S152–S173 (2007).

Supplementary Information is available in the online version of the paper.

Acknowledgements Epicentres and magnitudes of seismic events were obtained from the NEIC catalogue. Seismic waveform data presented in Supplementary Information were obtained from the Incorporated Research Institutions for Seismology (IRIS) Data Management Center. We thank T. Hanks, R. Harris, A. Michael, T. Parsons and P. Stark for their comments on a preliminary draft. V.S. works under contract at the US Geological Survey.

Author Contributions F.F.P. initiated the study and performed all seismic-wave analysis. F.F.P., R.S.S. and V.S. contributed equally to earthquake catalogue analysis. All authors discussed the results and helped write the manuscript.

Author Information Reprints and permissions information is available at www.nature.com/reprints. The authors declare no competing financial interests. Readers are welcome to comment on the online version of the paper. Correspondence and requests for materials should be addressed to F.F.P. (fpollitz@usgs.gov).

©2012 Macmillan Publishers Limited. All rights reserved

METHODS

Magnitude of completeness. The magnitude of completeness M_c of the NEIC catalogue has evolved over time. Supplementary Fig. 3 shows cumulative seismicity rates and the corresponding b values determined over three consecutive 10-yr time periods. The 1982–1992 seismicity rates are generally lower than rates since 1992. The global $M \geq 5.5$ seismicity rates have been essentially stable since 1992, the 1992–2002 rates diverging from the 2002–2012 values only for $M < 5.5$. This and the estimated b values and quality of the linear fits leads us to conclude that $M_c = 5.5$ is appropriate for the NEIC catalogue since 1992. A value of $M_c = 4.8$ is appropriate for the period between the 2004 Sumatra mainshock and the 2012 mainshock (see section on low pre-earthquake seismicity rate). Comparison of regional seismicity catalogues with the NEIC catalogue suggests that a value of $M_c = 4.5$ is appropriate for at least the past year.

Background seismicity rates. For the six $M \geq 8.5$ mainshocks of the past 10 yr, the $M \geq 5.5$ global seismicity rates presented in Fig. 2 are determined by excluding spherical caps of radius 1,500 km about a given mainshock epicentre for a particular time window. This procedure—applied equally to the pre-mainshock and post-mainshock periods—effectively removes the vast majority of aftershocks following the mainshocks, leaving only the remote seismicity in both the pre-mainshock and post-mainshock periods. In the main text, this procedure was applied separately to the specified periods preceding and following each mainshock, resulting in running-average remote seismicity rates from 10 d before to 10 d after a mainshock as well as 10-d pre-mainshock average remote seismicity rates. The latter may be considered 'background' remote seismicity rates, but the question arises as to the level and statistical fluctuations of this background using a longer catalogue.

Here we address the statistics of background seismicity rates using longer time intervals and with a Monte Carlo simulation approach. For this purpose, we use the NEIC catalogue for the period April 1992 to April 2012, extracting all events with $M \geq 5.5$ and depth $\leq$100 km. To render the estimation of background rates comparable with pre-mainshock rates presented in the main text, it is appropriate to de-cluster the catalogue. In doing so, we are guided by the fact that none of the six very large mainshocks was preceded by an event of magnitude $M > 8.1$ during the preceding 20 d. (The 26 December 2004 $M = 9.2$ Sumatra earthquake was preceded by the 23 December 2004 $M = 8.1$ Tasman Sea event.) Our strategy for de-clustering is to extract from the catalogue all sets of 10-d-long periods $(t - 10\,\mathrm{d}, t)$ such that no event of magnitude greater than $M_{\min}$ occurs in the 20 d preceding t. This is designed to remove time intervals that contain or are preceded by large-magnitude events. Compared with Gardner and Knopoff de-clustering[33], it uses a more restrictive spatial exclusion zone (infinite distance) but a less restrictive temporal exclusion zone. In order to mimic the sampling process of five very large mainshocks (that is, all the $M \geq 8.5$ events excluding the 2012 event) in one realization, five of these sets are drawn randomly and the rates of $M \geq 5.5$ events occurring in them averaged. That is, if there are N available 10-d sets, then one realization yields the estimate

$$R = \frac{1}{5}\sum_{i=1}^{5} \bar{R}_{v(i)}$$

where $\bar{R}_n$ is the average rate in set n and $v(i)$ is random variable uniformly distributed over the integers 1 through N. This process is repeated 100,000 times to generate a probability distribution of R.

Resulting probability distributions of R are shown in Supplementary Fig. 4. There is a decrease in the mean rate of $M \geq 5.5$ earthquakes from $\bar{R} = 1.20$ events per day in the unedited catalogue (Supplementary Fig. 4a) to $\bar{R} = 1.12$ events per day in the de-clustered catalogue with $M_{\min} = 8.1$ (Supplementary Fig. 4b). The value $\bar{R} = 1.12$ and corresponding 5% and 95% empirical probability bounds of 0.82 and 1.47 events per day define the grey region plotted in Fig. 2b.

The entire procedure may be repeated by sampling all available 10-d averages once, that is,

$$R = \bar{R}_n \ (n = 1, \ldots, N)$$

to replicate the averaging process used for the 2012 mainshock alone. The resulting $\bar{R}$ and corresponding 5% and 95% empirical probability bounds for this case define the grey region plotted in Fig. 2a.

Seismicity rate change. The question of the significance of the observed short-term rate increases in remote seismicity following $M \geq 8.5$ mainshocks (Fig. 2) was previously addressed over essentially all distance ranges using a large set of $M \geq 7$ mainshocks[11]. To answer it we must characterize the probability distribution of the change in the remote seismicity rate, with 'remoteness' being referenced to a set of $M \geq 7$ mainshocks. In doing so, our approach is similar to that of ref. 11, but we focus on the remote seismicity rate change.

We again use the NEIC catalogue for the period April 1992 to April 2012, extracting all events with $M \geq 5.5$ and depth $\leq$100 km. There are 243 $M \geq 7$ mainshocks during this period. For each mainshock of $M \geq 7$ considered separately, we define a spherical cap of angular radius 1,500 km about its epicentre and exclude all events within that zone. We may further de-cluster this 'unedited catalogue' according to the prescription given in the preceding section: for a given $M_{\min}$, mainshocks with any $M \geq M_{\min}$ event within 20 d preceding it are excluded. We then evaluate the average seismicity rate in the preceding 10 d (R_{pre}) and the following 2 d (R_{post}), and define the seismicity rate change $\Delta R = R_{\mathrm{post}} - R_{\mathrm{pre}}$ (equation (1) of main text). To mimic the sampling process of one or five very large mainshocks, we follow the Monte Carlo approach described in the preceding section.

Resulting probability distributions of ΔR for one mainshock are shown in Supplementary Fig. 5. In the two considered cases, there is a statistically insignificant average rate decrease ($\Delta\bar{R} = -0.03$ events per day for the unedited catalogue in Supplementary Fig. 5a; $\Delta\bar{R} = -0.06$ events per day for the de-clustered catalogue in Supplementary Fig. 5b). The 95% upper bound on the empirical probability distribution for a rate increase for a single mainshock is 1.25 events per day for both the unedited and the de-clustered catalogues. Similarly, the 95% upper bound on the empirical probability distribution for a rate increase for an aggregate of five mainshocks is 0.55 events per day for both the unedited and the de-clustered catalogues (Supplementary Fig. 6).

It is of interest to understand the ranges of R_{pre} and R_{post} separately as well as their covariance for the considered set of $M \geq 7$ mainshocks. Supplementary Fig. 7a shows the distributions of R_{pre} and R_{post} obtained through the above Monte Carlo scheme for a single event with $M_{\min} = 8.1$. The 95% empirical upper bound on R_{post}, equal to 2.75 events per day, is much higher than the corresponding upper bound on ΔR, equal to 1.25 events per day (Supplementary Fig. 5b). The primary reason is that the means of R_{pre} and R_{post} are almost identical, such that the distribution of ΔR is centred on a near-zero mean (Supplementary Fig. 5b). In addition, R_{pre} and R_{post} are moderately correlated, such that the variance of their difference is slightly smaller than the variance of either quantity alone. The same is true for the 95% upper bound on R_{post} for an aggregate of five events (Supplementary Fig. 7b), equal to 1.65 events per day, which is much higher than the corresponding upper bound on ΔR, equal to 0.55 events per day (Supplementary Fig. 6b).

Distance dependence of global seismicity. We characterize the global seismicity following the six very large mainshocks in terms of the distances of $M \geq 5.5$ events from the respective mainshock epicentres. This is displayed graphically in Supplementary Fig. 8 in terms of event rates per unit area in logarithmic distance bins for each of three post-mainshock time intervals and a single pre-mainshock interval. For both the 11 April 2012 $M = 8.6$ mainshock and the other five $M \geq 8.5$ mainshocks, post-mainshock global seismicity rates are systematically higher than pre-mainshock rates at remote distances, that is, well beyond the near-field aftershock zone.

Calculation of the cumulative number of $M \geq 4.5$ remote events. We extract from the NEIC catalogue all events of depth $\leq$100 km and $M \geq 4.5$, and construct three subsets of events: those in the 6 d preceding the 2012 mainshock, those in the 6 d following the 2012 mainshock and those within 6-d intervals following $M \geq 7$ events during the year preceding the 2012 event. To restrict attention to remote events, we exclude all events lying within a spherical cap of radius 1,500 km from the 2012 centroid (first and second cases) or a given $M \geq 7$ mainshock (third case, that is, background 'remote' events). The cumulative numbers of events as functions of magnitude for these three cases are compared in Fig. 3.

Smaller mainshock–aftershock sequences. Both pre-mainshock and post-mainshock rates in Fig. 2 may be influenced by clustering from smaller mainshock–aftershock sequences. Better to assess the remote seismicity pattern without such clustering, it is expedient to remove smaller mainshock–aftershock sequences. We do so by applying an additional filter to recalculate the 2-d running-average seismicity rates, by further excluding any event that is preceded by an $M \geq 5.5$ event during the previous 24 h and within a 100-km radius. Resulting seismicity rates for the 30-d periods preceding and following the $M \geq 8.5$ mainshocks are shown in Supplementary Fig. 2. The ~-2-d heightened remote seismicity following all mainshocks is seen to be anomalous over the entire time period, showing that these increased seismicity rates are not attributable to induced smaller mainshock–aftershock sequences.

Low pre-earthquake seismicity rate. Seismicity rates were exceptionally low in the days before the 2012 mainshock. To demonstrate this, we divided the NEIC catalogue into 6-d bins or 12-d bins, which yields sufficient sampling of $M \geq 4.8$ and $M \geq 5.5$ events, respectively. We measured the completeness level of the bins from the 2004 $M_w = 9.2$ Sumatra mainshock to the 2012 east Indian Ocean mainshock; $M_c \leq 4.8$ for 95% of the 6-d bins. Using either the $M = 4.8$ or the $M = 5.5$ threshold, we find that the number of events during the bin preceding the 2012 mainshock is the ninth lowest at $M \geq 4.8$ and the lowest at $M \geq 5.5$ for a 7.3-yr period (Fig. 4). In other words, respectively 98.4% or 100% of the bins had a higher

©2012 Macmillan Publishers Limited. All rights reserved

background rate, such that the global seismicity rates preceding the 2012 event were exceedingly low compared with the prevailing rates over these 7.3 yr.

Calculation of global seismic wavefields. Seismic wavefields are calculated using the direct Green's function method of ref. 34 on the spherically symmetric isotropic PREM model[35]. Global seismic wavefields are calculated using a point-source approximation of the 11 April 2012 mainshock convolved with a source time function consisting of a cosine ramp function of duration 100 s, and low-pass filtered at 80 s. The source epicentre, depth and moment tensor we use are that of the Global CMT Solution[30]: 2.24° N, 92.78° E; 40 km; $M_{rr} = 0.136 \times 10^{29}$ dyn cm, $M_{tt} = -0.591 \times 10^{29}$ dyn cm, $M_{pp} = 0.455 \times 10^{29}$ dyn cm, $M_{rt} = -0.396 \times 10^{29}$ dyn cm, $M_{rp} = 0.046 \times 10^{29}$ dyn cm, $M_{tp} = -0.615 \times 10^{29}$ dyn cm. Although the actual rupture is much more complex[14–18], at these long periods our simple model captures the first-order character of the global seismic wavefield (Supplementary Fig. 9).

33. Gardner, J. K. & Knopoff, L. Is the sequence of earthquakes in southern California, with aftershocks removed, Poissonian? *Bull. Seismol. Soc. Am.* **64,** 1363–1367 (1974).
34. Friederich, W. & Dalkolmo, J. Complete synthetic seismograms for a spherically symmetric earth by a numerical computation of the Greens function in the frequency domain. *Geophys. J. Int.* **122,** 537–550 (1995).
35. Dziewonski, A. M., Chou, T.-A. & Woodhouse, J. H. Determination of earthquake source parameters from waveform data for studies of global and regional seismicity. *J. Geophys. Res.* **86,** 2825–2852 (1981).

©2012 **Macmillan Publishers Limited. All rights reserved**

doi:10.1038/nature11504

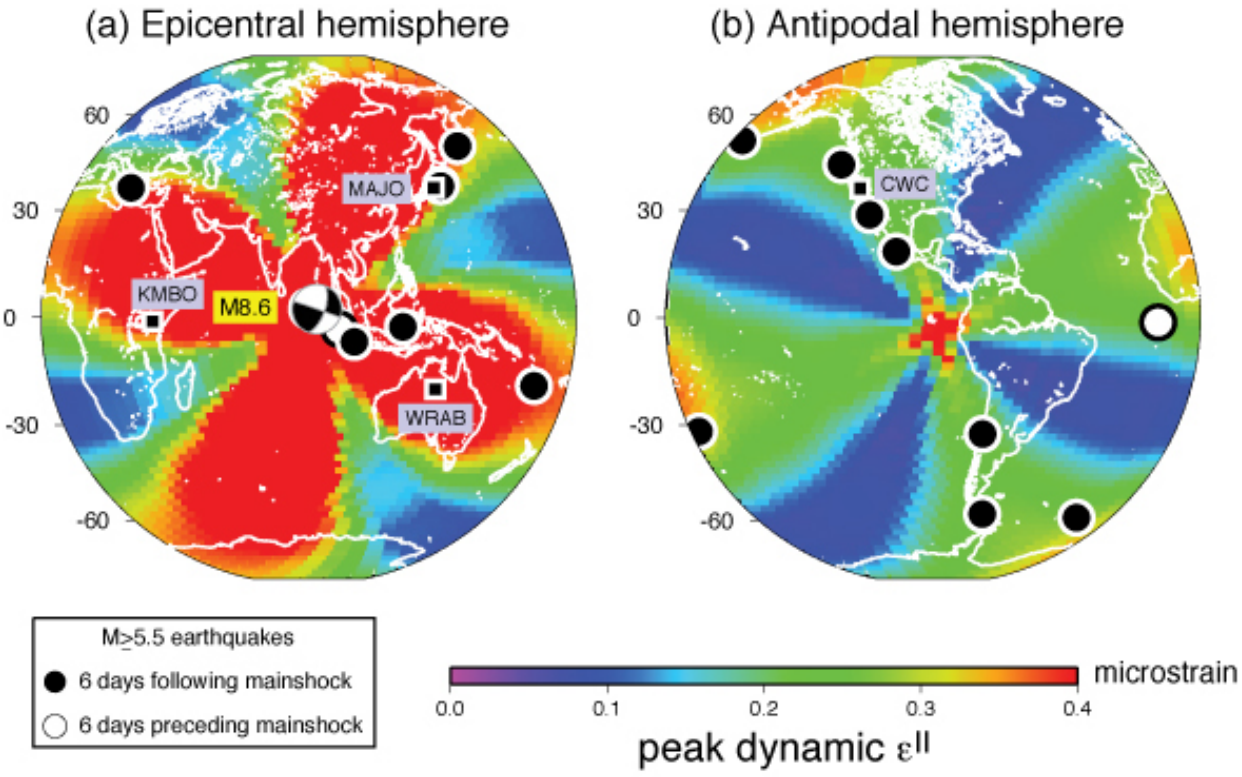

Figure S-1: **Global maps of the peak ϵ^{II} (the square root of the second invariant of the deviatoric strain tensor) imparted by the mainshock during seismic wave propagation** (see **Methods summary**). Superimposed are the epicenters of $M \geq 5.5$ events which occurred during the six days preceding the mainshock (2 white circles) and following the mainshock (24 black circles, 16 of which are remote, i.e. > 1500 km from the mainshock). The focal mechanism of the mainshock is plotted at its epicenter. Broadband seismic stations are indicated with a black square and light blue station labels.

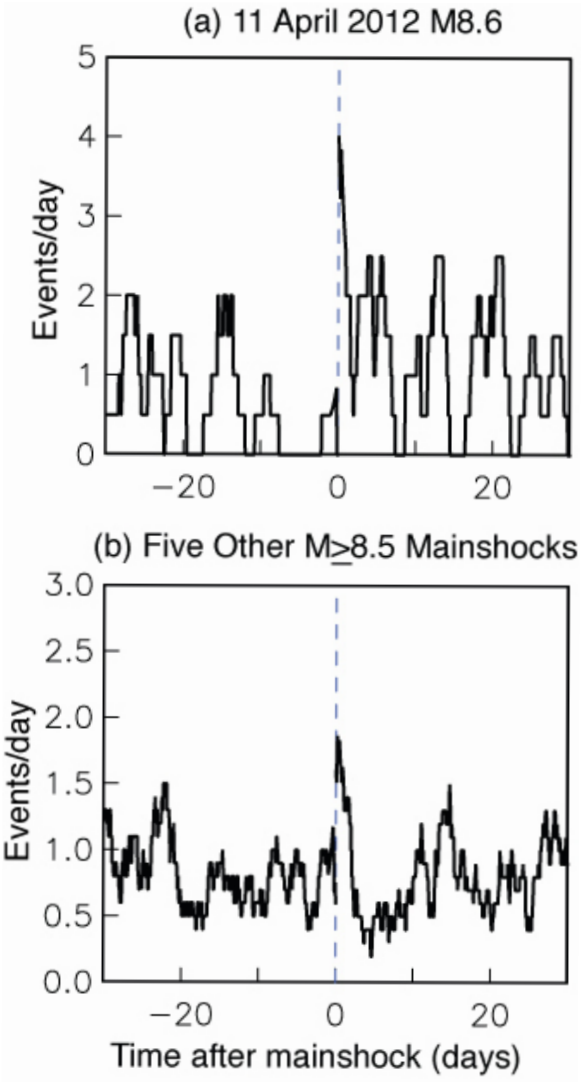

Figure S-2: **Global rates of shallow (depth $\leq$ 100 km) $M \geq 5.5$ earthquakes during the 30 days preceding and following a mainshock.** A running average of half-width of one day is used to construct each curve (see **Methods summary**). Time is relative to the mainshock origin time. (a) 11 April 2012 M8.6 East Indian Ocean mainshock. (b) A collection of five other mainshocks of magnitude $M \geq 8.5$ (Table 1). Events within 1500 km of the mainshock are excluded, and small mainshock-aftershock sequences are also excluded (**Smaller Mainshock-Aftershock Sequences** section of **Methods**).

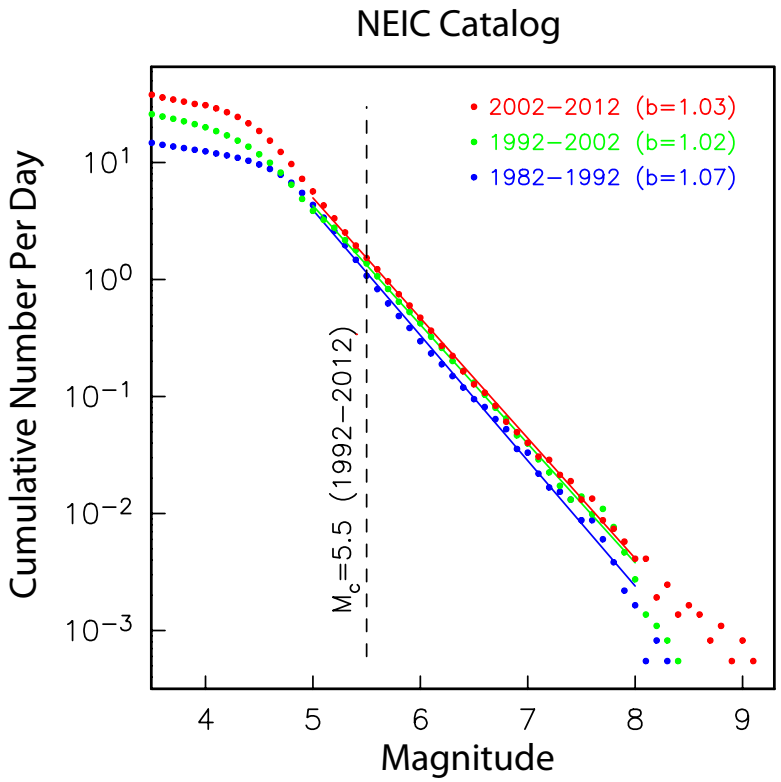

Figure S-3: **Cumulative number of global $M \geq 3.5$ events of depth ≤ 100 km during the three indicated 10-year periods.** Corresponding $b-$ values are derived from linear fits over the $5 \leq M \leq 8$ range.

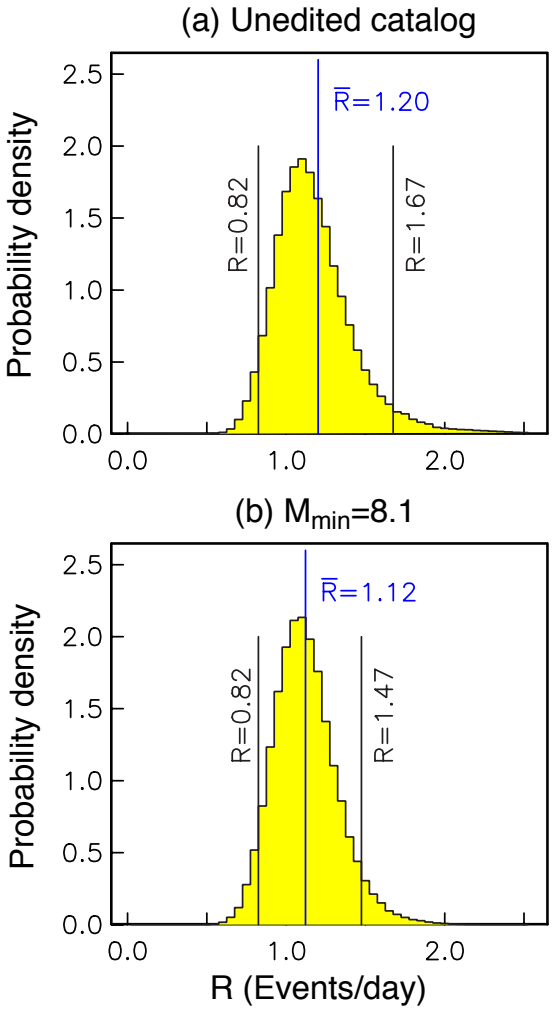

Figure S-4: **Empirical probability density functions of the rate of $M \geq 5.5$ earthquakes for an aggregate of five 10-day intervals.** They are calculated using the sampling and averaging procedure discussed in the **Background Seismicity Rates** section of **Methods**. $M_{\min}$ is the magnitude used for declustering the NEIC catalog, i.e. to restrict 10-day-long sampling interval to those that have no event exceeding a magnitude $M_{\min}$ within 20 days preceding the end of the interval. $\bar{R}$ denotes the mean value of R, and vertical bars denote locations of the 5% and 95% bounds of the distributions. $\bar{R}$ and these bounds for the declustered catalog in (b) define the gray region in Fig. 2b of the main text.

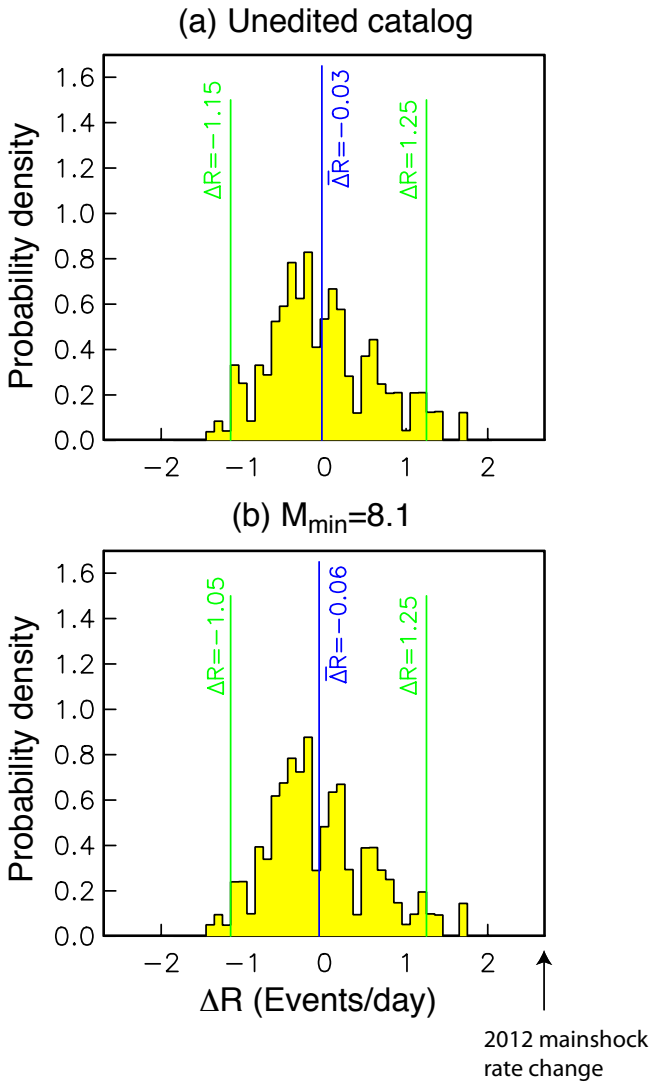

Figure S-5: **Empirical probability density functions of the seismicity rate change ΔR for one $M \geq 7$ mainshock.** They are calculated using the sampling and averaging procedure discussed in the **Seismicity Rate Change** section of **Methods**. $M_{\min}$ is the magnitude used for declustering the NEIC catalog. $\bar{\Delta R}$ denotes the mean value of ΔR, and vertical bars denote locations of the 5% and 95% tails of the distributions. The observed rate change associated with the 2012 mainshock is 2.7 events/day.

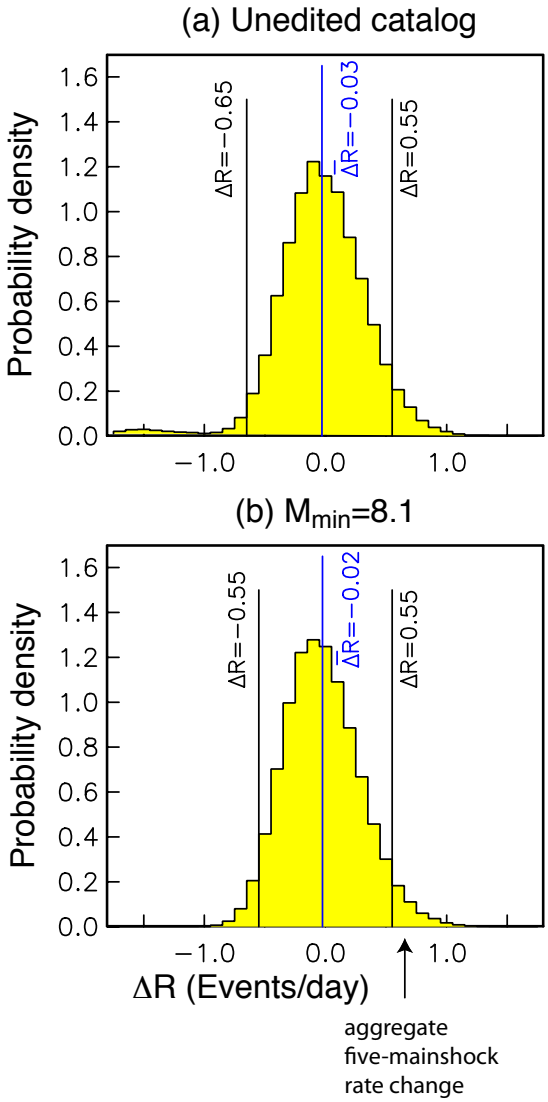

Figure S-6: **Empirical probability density functions of the seismicity rate change ΔR for an aggregate of five $M \geq 7$ mainshocks.** They are calculated using the sampling and averaging procedure discussed in the **Seismicity Rate Change** section of **Methods**. $M_{\min}$ is the magnitude used for declustering the NEIC catalog. $\bar{\Delta R}$ denotes the mean value of ΔR, and vertical bars denote locations of the 5% and 95% tails of the distributions. The observed rate change associated with the aggregate five pre-2012 mainshocks (Table 1 of main text) is 0.65 events/day.

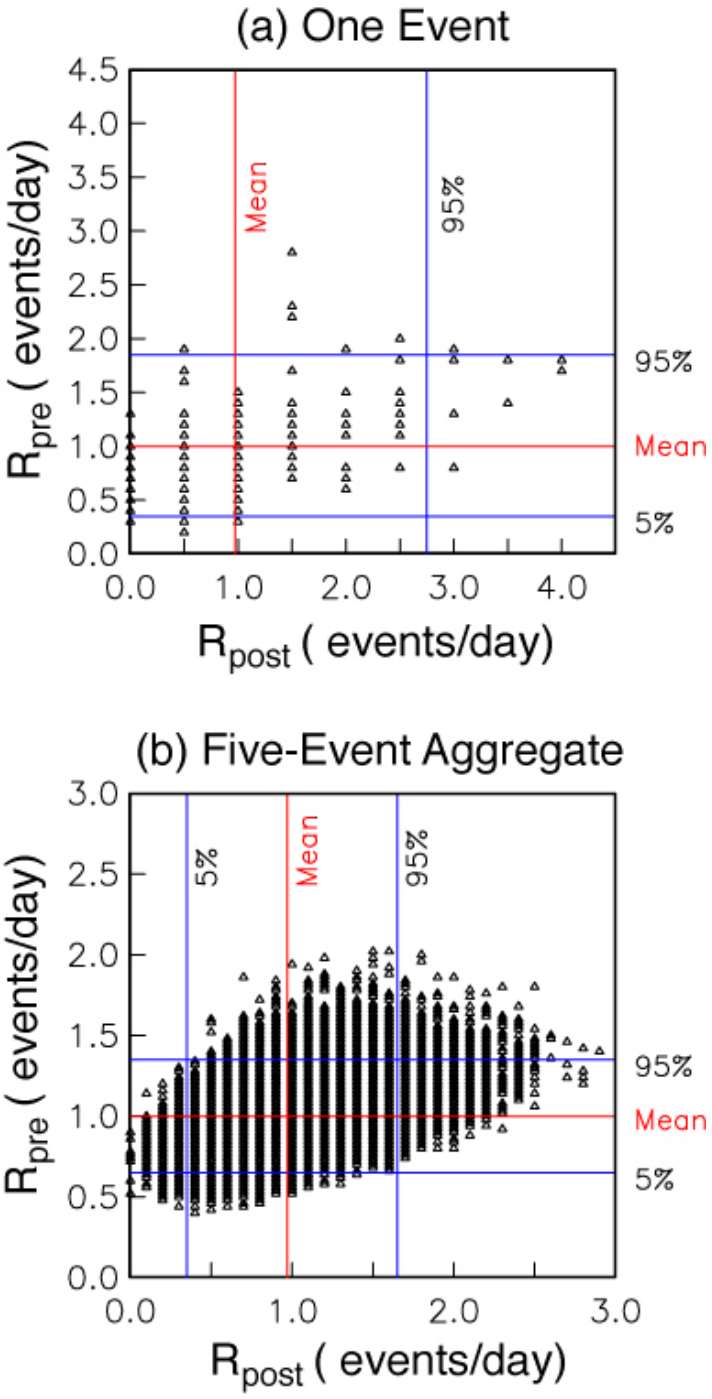

Figure S-7: **Distributions of pre-mainshock and post-mainshock seismicity rates $R_{\rm pre}$ and $R_{\rm post}$.** These distributions are obtained in a Monte Carlo simulation of one $M \geq 7$ catalog event through eqn 3 (a) or an aggregate of five $M \geq 7$ catalog events through eqn 2 (b). Means and 5th and 95th percentiles of the marginal distributions of these rates are indicated; the fifth percentile for the distribution of $R_{\rm post}$ in (a) lies within the samples of $R_{\rm post} = 0$ and is therefore omitted. Note that in (a) $R_{\rm pre}$ and $R_{\rm post}$ are quantized in units of 0.1 or 0.5 events/day, respectively, because of the 10 day and 2 day sampling intervals. In both (a) and (b), one or more realizations may plot on the same triangle (the figure does not convey the density of outcomes of the realizations).

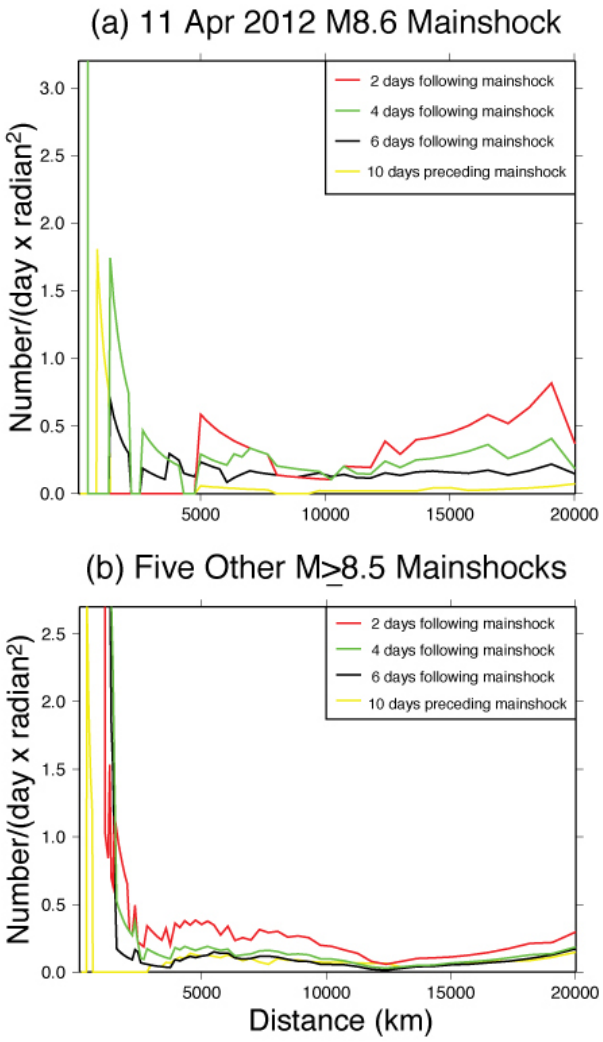

Figure S-8: **Distribution of pre-mainshock and post-mainshock seismicity with respect to epicentral distance Δ at magnitude $M \geq 5.5$.** Event counts are calculated using a running average over overlapping logarithmic distance intervals, then divided by the area contained in that interval. At a given ordinate value Δ' in degrees, the events are counted within the interval $\log_{10}\Delta = (\log_{10}\Delta' - 0.1, \min\{\log_{10}\Delta' + 0.1, \log_{10} 180\})$. Separate distributions are shown for the 2012 East Indian Ocean event (a) and five other mainshocks of magnitude $M \geq 8.5$ of the past 10 years (b). Various curves represent seismicity rates per unit area averaged over the indicated time intervals.

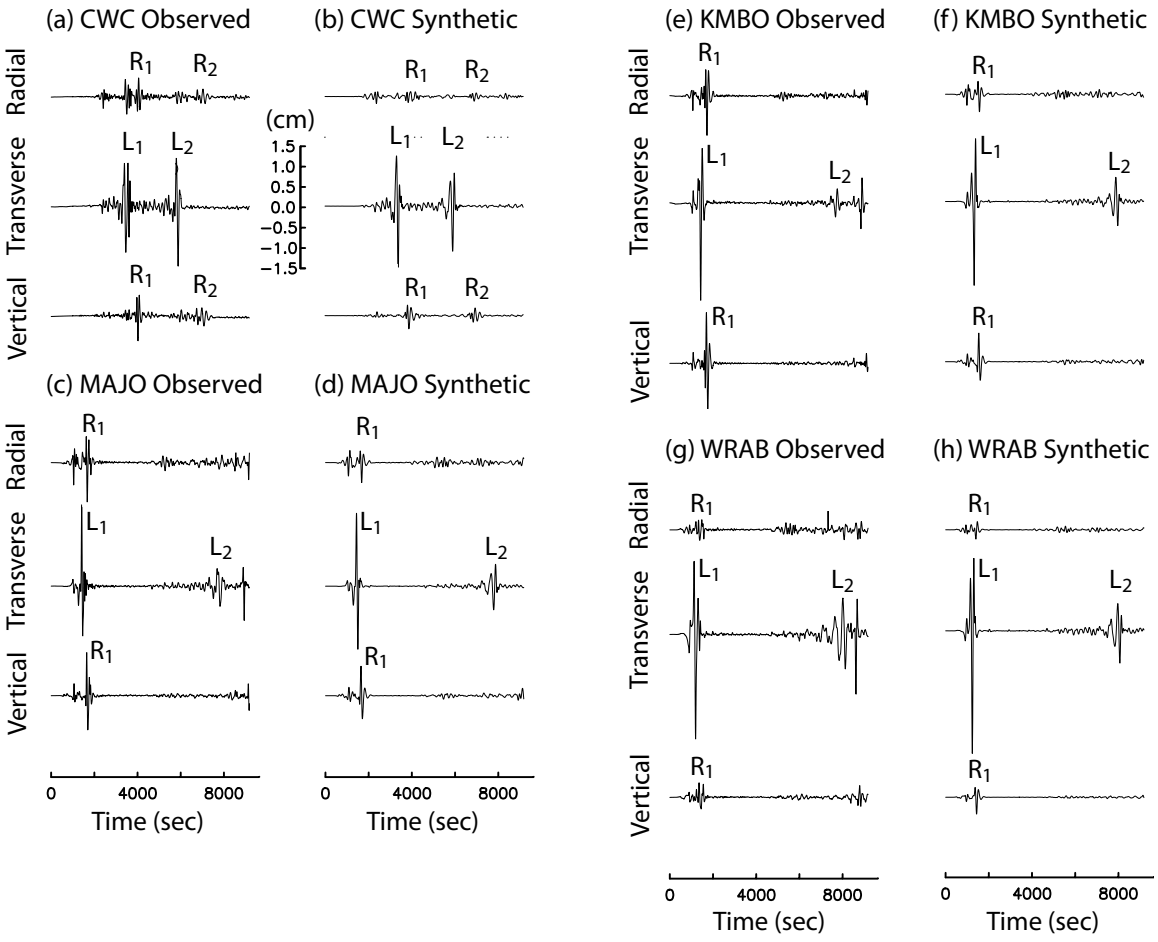

Figure S-9: **Comparison of observed and synthetic seismograms for the 11 April 2012 M8.6 event.** Observed (a,c,e,g) and synthetic (b,d,f,h) displacement seismograms are presented at broadband stations CWC in California (USA), MAJO in Japan, KMBO in Kenya, and WRAB in Australia. Station locations are indicated in Fig. 1 of the main text. The largest displacements are realized during passage of the L_1 and L_2 wave trains. Arriving at $\sim$ 9000 sec on the observed MAJO, KMBO, and WRAB seismograms are the L_1 and R_1 arrivals of the M8.2 aftershock which occurred 2 hours and 5 minutes after the M8.6 mainshock.

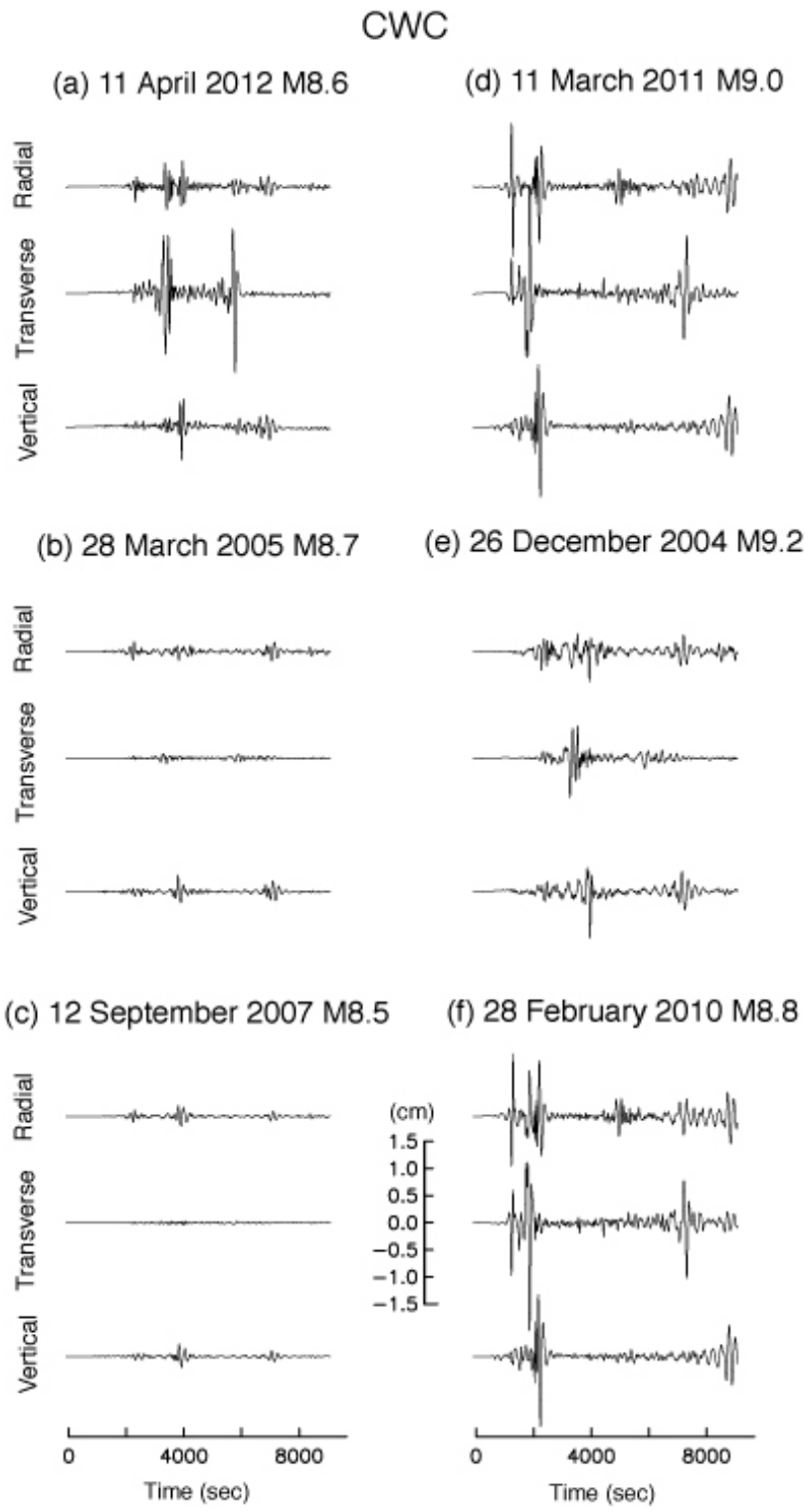
CWC
(a) 11 April 2012 M8.6
(d) 11 March 2011 M9.0
Radial
Transverse
Vertical
(b) 28 March 2005 M8.7
(e) 26 December 2004 M9.2
(c) 12 September 2007 M8.5
(f) 28 February 2010 M8.8
(cm)
1.5
1.0
0.5
0.0
−0.5
−1.0
−1.5
0
4000
8000
Time (sec)

Figure S-10

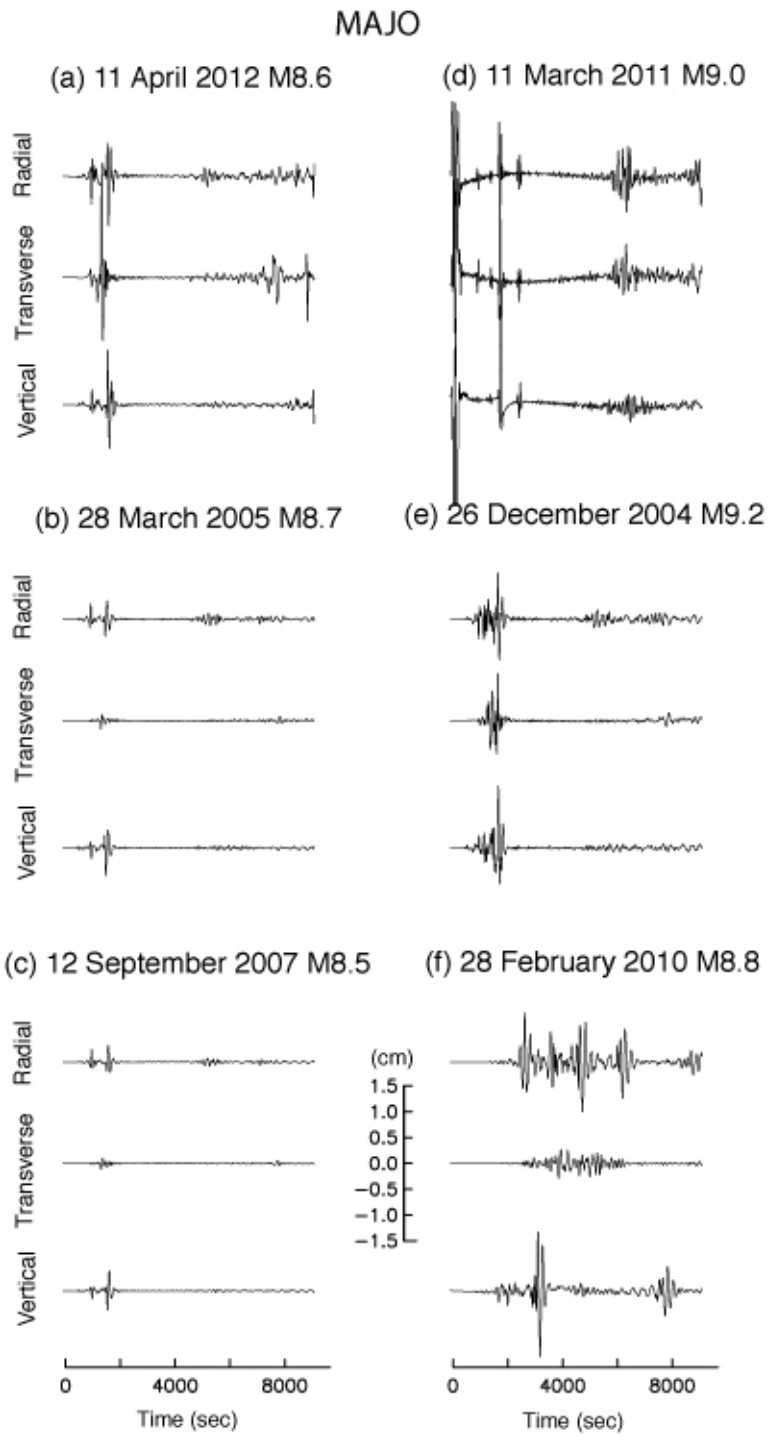

Figure S-10: (continued)

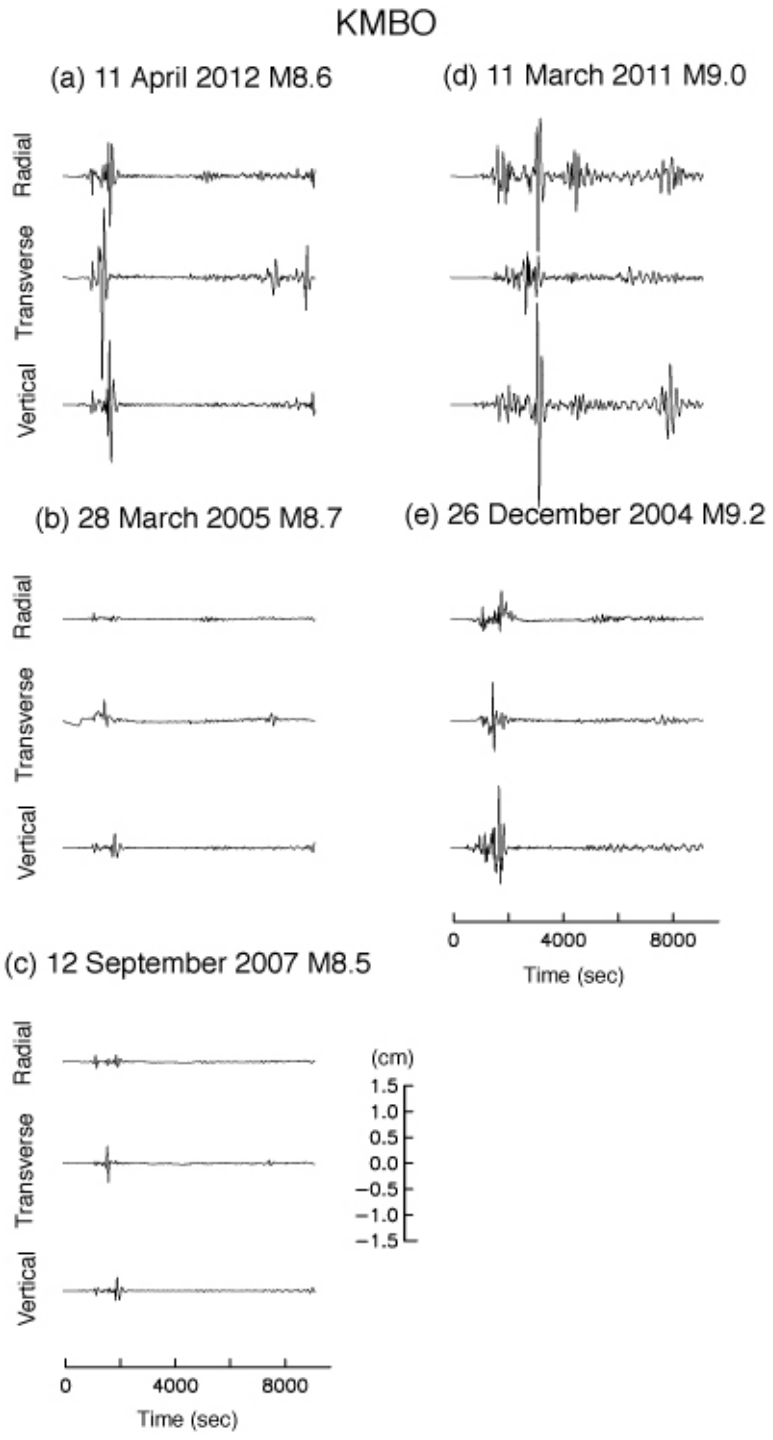

Figure S-10: (continued)

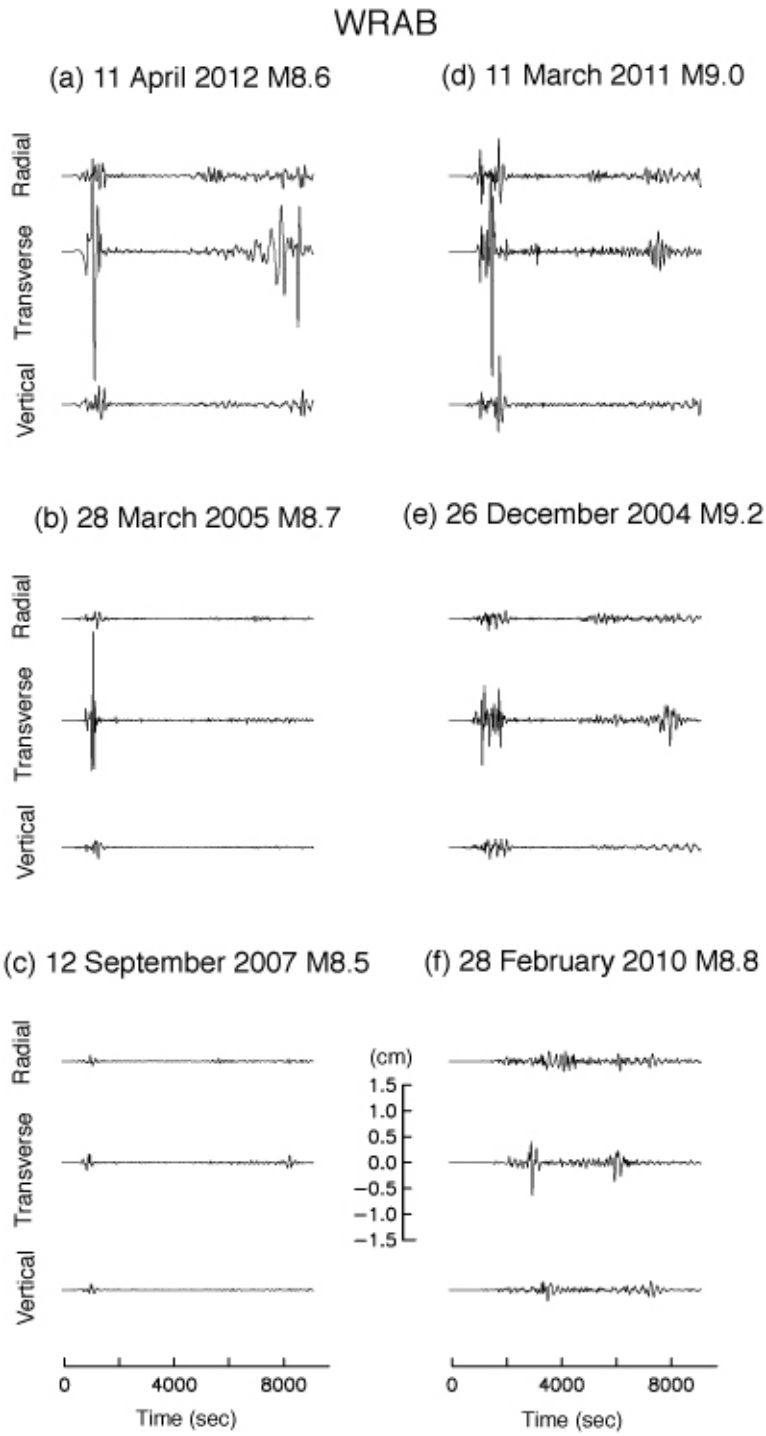

Figure S-10: **Displacement seismograms of six $M \geq 8.5$ events at selected broadband stations.** (a) 11 April 2012 Indian Ocean earthquake, (b) 28 March 2005 Nias, (c) 12 September 2007 M8.5 Sumatra, (d) 11 March 2011 Tohoku earthquake, (e) 26 December 2004 M9.2 Sumatra, and (f) 27 February 2010 M8.8 Maule, Chile. Separate plots are shown for stations CWC, MAJO, KMBO, and WRAB (locations shown in Fig. S-1). The three-component seismograms are resolved onto the radial, transverse, and vertical components and low-pass filtered at 80 sec period.

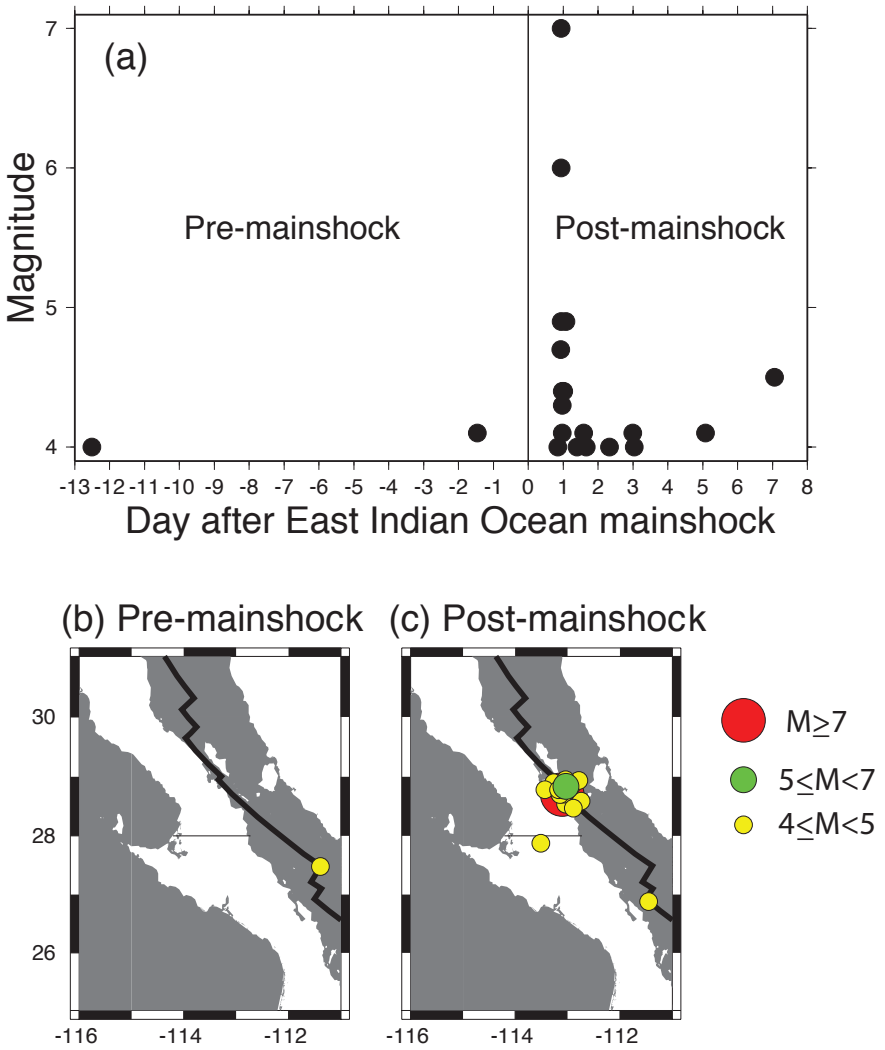

Figure S-11: **Seismicity in the Gulf of California from 30 days before to 30 days after the 2012 M8.6 mainshock.** In (a), there is no NEIC catalog seismicity in the -30 to -13 day or +8 to +30 day intervals. This data indicates a $\sim$ 100-fold increase in seismicity: there were two events in the preceding 30 days, and 13 events in the following 2 days. Two of the $M < 5$ post-mainshock events occurred before the larger M6.0 and M7.0 events and are thus not local aftershocks.